719941

ORNL-4720
UC-41 – Health and Safety

Contract No. W-7405-eng-26

HEALTH PHYSICS DIVISION ANNUAL PROGRESS REPORT

For Period Ending July 31, 1971

K. Z. Morgan, Director

W. S. Snyder, Assistant Director
E. G. Struxness, Assistant Director

OCTOBER 1971

REPOSITORY MMES/X-10/Vault
COLLECTION Central Files
BOX No. ORNL-4720
FOLDER

OAK RIDGE NATIONAL LABORATORY
Oak Ridge, Tennessee 37830
operated by
UNION CARBIDE CORPORATION
for the
U.S. ATOMIC ENERGY COMMISSION

1147990

A-00390
Human Studies Project

Contents

SUMMARY vii

PART I. RADIOACTIVE WASTE DISPOSAL

1. FATE OF TRACE ELEMENTS AND RADIONUCLIDES IN TERRESTRIAL ENVIRONMENT 1

Evaluation of Zonal Centrifugation Techniques 1

Applications of Zonal Centrifugation 3

Heavy Metal Distribution in Streams and Rivers 7

Walker Branch Watershed Studies 9

2. DISPOSAL BY HYDRAULIC FRACTURING 11

Investigations at Oak Ridge 11

Investigations in New York State 11

3. DISPOSAL IN NATURAL SALT FORMATIONS 14

Stratigraphy and Structure of the Rocks at the Proposed Federal Repository, Lyons, Kansas 14

4. ENGINEERING, ECONOMIC, AND SAFETY EVALUATIONS 20

Siting and Operation of Nuclear Facilities 20

5. DOSE ESTIMATION STUDIES RELATED TO PEACEFUL USES OF NUCLEAR EXPLOSIVES AND OTHER RADIONUCLIDE RELEASES 23

Utilization of Natural Gas from Nuclearly Stimulated Wells 23

Development of Radiation Safety Guides for Environmental Releases of Radioactivity 24

A General Model to Estimate Dose to Man from Radionuclide Deposition 26

The Transfer of Tritium to Man after Wet Deposition 28

PART II. RADIATION PHYSICS

6. THEORETICAL RADIATION PHYSICS 30

Effect of Lateral Scattering on Dose from 400-MeV Protons and Neutrons 30

Semiclassical Estimation of Neutron Stopping Power 31

Z_1^3 Effect in the Stopping Power of Matter for Charged Particles 31

1147991

Contribution of Surface Losses to the Stopping Power of Matter for Charged Particles 33
Dosimetric Field Quantities in Health Physics 34
What Is "Energy Imparted"? 34
Reexamination of Scattering by a Pair of Fixed Dipolar Charges 34
Critical Binding of an Electron to a Rotationally Excited Dipolar System 35
Unlocalized Energy Losses by Charged Particles in Matter 37
Electron Slowing-Down-Cascade Spectra in Solids 37
Volume Plasmon Decay 39
Photon Interactions at a Rough Metal Surface 40
Dosimetry of Pion Beams 40

7. INTERACTION OF RADIATION WITH LIQUIDS AND SOLIDS 42
Optical Properties of Rubidium above the Plasma Energy 42
Optical Properties of Uranium Mononitride 43
Study of the Optical Properties of Solids by Ellipsometry 44
High-Energy X-Ray Satellites of the L_{23} Emission Bands of Na, Mg, Al, and Si 46
Soft X-Ray Emission Spectra of MgO and MgF_2 47
Photoelectron Attenuation Lengths in Aluminum 48
Photoelectric Manifestation of the Optical Plasmon Resonance in Magnesium 50

8. PHYSICS OF TISSUE DAMAGE 51
Electron-Slowing-Down Studies 51
Optical Properties of Organic Liquids 52

9. ELECTRON AND ION COLLISION PHYSICS 56
Electron Impact Excitation and Ionization of the Rare Gases 56
Thermal and Near-Thermal Electron Attachment Rate and Transport Coefficients for Oxygen with a Modified Time-of-Flight Method 57
Electron Interactions with Carbonyl Compounds 60
Ionic Processes in Boron Halides 62
Collisional Ionization of Cesium by O_2, NO_2, and N_2O: Determination of Electron Affinities 63
FSU-ORNL Chemical Accelerator 67

10. ATOMIC AND MOLECULAR RADIATION PHYSICS 69
Swarm-Determined Electron Attachment Cross Sections as a Function of Electron Energy 69
Cross-Section Functions for Electron Attachment Resonances with Cross Sections Increasing Sharply at Thermal Energies 71

1147992

Dissociative Electron Attachment to Halogenated Aliphatic Hydrocarbons 72

Electron Capture of Molecules Forming "Moderately Short-Lived" Negative Ions under High-Gas-Pressure Conditions 72

Lifetimes of Long-Lived Polyatomic Negative Ions 73

Scattering of Slow Electrons by π-Electron-Containing Organic Molecules 73

Threshold Electron Excitation of Molecules: Location of Triplet and Compound Negative-Ion States 73

Quasi-Equilibrium Theory of Unimolecular Decompositions 73

Ionic Fragmentation through Centrifugal Barriers 74

Linking of Existing Data on Electron Attachment in Gases with Those in the Liquid Phase 74

Photophysical Studies of Organic Liquids and Solutions: Emission Spectra from Higher Excited π-Singlet States of Aromatic Hydrocarbons in Solution 76

11. GRADUATE EDUCATION AND VOCATIONAL TRAINING 78

Part III. RADIATION DOSIMETRY RESEARCH

12. DOSIMETRY FOR HUMAN EXPOSURES AND RADIOBIOLOGY 80

Japanese Dosimetry Program 80

Calculations of Dose and LET Distributions for Neutrons and Gamma Rays 81

Measurements of Dose Distributions 90

13. APPLIED DOSIMETRY RESEARCH 95

TSEE Research 95

Thermoluminescence Dosimetry 103

Nuclear Track Etching Studies 104

14. INTERACTION OF CHARGED PARTICLES WITH MATTER 107

15. SPECTROMETRY RESEARCH AND DEVELOPMENT 110

Organic Scintillator Research 110

A Voltage-to-Frequency Converter 110

Health Physics Research Reactor Timer 111

16. HPRR AND ACCELERATOR OPERATIONS 112

Health Physics Research Reactor Operations 112

Intercomparison Studies 112

Accelerator Operations 114

A Self-Replenishing Tritium Target 114

1147993

PART IV. INTERNAL DOSIMETRY

17. PRELIMINARY INDICATIONS OF THE AGE VARIATION OF THE SPECIFIC ABSORBED FRACTION FOR PHOTONS 116

18. DOSE TO A DEVELOPING FETUS FROM A GAMMA EMITTER IN THE BLADDER 119

19. ABSORBED FRACTIONS FOR INTERNAL EMITTERS 121

20. DEPTH-DOSE RATES IN REFERENCE MAN FROM ELECTRONS AND BETA PARTICLES IN A RADIOACTIVE CLOUD 125

21. ESTIMATES OF MICROCURIE-DAYS RESIDENCE, DOSE EQUIVALENT, AND $(MPC)_w$ FOR THORIUM-232 IN MAN USING A MAMMILLARY MODEL 128

THESES, PAPERS, PUBLICATIONS, AND LECTURES

THESES 132

PAPERS 133

PUBLICATIONS 138

LECTURES 148

1147994

Summary

PART I. RADIOACTIVE WASTE DISPOSAL

1. Fate of Trace Elements and Radionuclides in Terrestrial Environment

The development and application of zonal centrifugation to soil and sediment analyses were continued. Adsorption of polyvinylpyrrolidone on montmorillonite interlayers was demonstrated. Gypsum was segregated and identified in a calcareous Holtsville soil from California. The sensitivity of the zonal centrifugation technique to quantifying minerals in soils is illustrated for the clay fraction of a Dodge soil. Bottom sediments of White Oak Lake could be banded by zonal centrifugation without appreciable dissolution of radionuclides, but the suspended sediments lost appreciable amounts in the less than 2-μ fraction.

Heavy metals were determined in the water and suspended sediments of several samples taken from a stream draining a mineralized zone. The bulk of the metal is transported in the dissolved state in the 1- to 25-ppb range. The concentration per unit weight of solid is about an order of magnitude higher in the particulates than in the dissolved solids.

2. Disposal by Hydraulic Fracturing

Almost no work was done with hydraulic fracturing at Oak Ridge during the reporting period. Work in New York consisted in making three "tagged" injections, each of 100,000 gal of water, at depths of 1450, 1226, and 1010 ft. All three injections formed horizontal fractures, but the third injection at 1010 ft also broke vertically downward about 400 ft and then moved horizontally out to the east. The formation of a vertical fracture was not unexpected. The pressure-decay curve from the first injection was unsatisfactory because only a poor gage was available. The analysis of the pressure-decay curve for the second injection showed a break at a pressure equal to the weight of the overburden. The pressure-decay curve from the third injection has not yet been analyzed.

3. Disposal in Natural Salt Formations

Geologic and hydrologic investigations at the proposed repository site have revealed that the rocks are all of sedimentary origin and, for the most part, are flat-lying. Rock salt, interbedded with clay shale and anhydrite stringers, lies between about 800 and 1100 ft below the surface. This salt section is capped with impermeable shales, while a thick sequence of shale and interbedded anhydrite lies directly beneath it. Two distinct freshwater aquifers are known to exist at depths of about 100 and 300 ft below the surface at the site.

4. Engineering, Economic, and Safety Evaluations

Investigation has continued of factors involved in the siting and operation of nuclear facilities. The influence of parent decay and daughter buildup on the potential radiation exposures downwind from a gaseous effluent illustrates the versatility of the atmospheric release computer code. From our search for potentially critical radionuclides at reactors, fuel reprocessing plants, and waste management facilities, a comprehensive nuclear data base has evolved. Computer codes permit rapid access and manipulation of the Nuclide and Biological Information System.

5. Dose Estimation Studies Related to Peaceful Uses of Nuclear Explosives and Other Radionuclide Releases

Studies of doses from the hypothetical use of Gasbuggy gas in areas served by El Paso Natural Gas Company were very nearly completed the past year, while similar investigations related to the Rulison project, the second experiment designed to test the nuclear stimulation concept, were just getting started at the end of the year.

An experiment was performed in a small natural gas processing plant near Barnhardt, Texas, in cooperation with El Paso Natural Gas Company to study the

1147995

distribution of tritiated hydrocarbons among plant products and to evaluate exposures that plant personnel may receive during the processing of natural gas containing tritium and ^{85}Kr. The maximum dose commitment received by plant personnel during the test was 0.7 millirem, and this was attributed to the handling of tritium for instrument calibration rather than breathing diluted plant fuel gas combustion products. Analysis of liquid and gas hydrocarbon samples, taken during and soon after the test, is not complete.

The Cumulative Exposure Index concept is being developed to facilitate realistic assessment of environmental releases of radioactivity. The aim of the concept is to assess the releases on the basis of time-integrated radionuclide concentrations measured in suitable environmental sampling media. Environmental pathway models and dose models are used to convert the measured environmental radionuclide concentrations into estimates of radiation dose to man. To complete the assessment, the estimates of dose are compared with basic radiation safety standards.

The methodology under development for assessing environmental radioactivity involves dynamic modeling techniques or systems simulations. A generalized model was constructed to simulate selected terrestrial pathways by which fallout radioactivity can be transferred to man. The model is intended for preliminary predictions of radionuclide intakes by man through consumption of milk, beef, and plant parts contaminated directly by fallout as well as by uptake from the soil. The model is sufficiently versatile that it can be applied to many terrestrial environments and to all radionuclides.

A specific model was developed to simulate the transfer of tritium to man after wet deposition. Tritium movement through the soil is simulated as a diffusion process. The model supports the conclusion that, except for the desert, the time-dependent concentration of tritium in the soil compartment is primarily determined by the rainfall after deposition, and it is essentially independent of the assumed compartment depth. A simple chart facilitates estimation of the total dose to man from a given wet deposition source and the subsequent rainfall rate.

PART II. RADIATION PHYSICS

6. Theoretical Radiation Physics

A classical impact parameter approach has been used to calculate a stopping-power correction term which depends on the sign of the charge of the incident particle.

An equation has been derived which may be used to estimate the energy loss due to the presence of foil surfaces and hence the relative contribution of surface losses to experimental measurements of stopping power.

The electron density fluctuation generated by a swift charged particle in a condensed medium has been investigated in order to elucidate the ultimate spatial distribution of initially unlocalized energy loss events. Electron slowing-down-cascade spectra generated by uniformly distributed high-energy electron sources in various solids are being determined theoretically in a program paralleling the experimental research being carried out in the Radiation Physics Section. The decay rate of volume plasmons in a nearly free-electron-like system has been determined using many-body perturbation theory techniques. The diffuse scatter and plasmon creation probability of photons incident on a rough bounding surface of a free electron gas has been studied theoretically.

Calculations were made to show the effects of lateral scattering on depth-dose curves for 400-MeV protons and neutrons. Also, an estimate of the stopping power of matter for neutrons shows that this quantity is expected to be smaller than that for protons by a factor of about 10^5. A Monte Carlo program was completed for the calculation of depth-dose curves from pion beams. Good agreement was obtained between calculated and experimental curves in water. The program is being used to study the effects of various beam characteristics of interest for cancer radiotherapy with negative pions.

The nature of critical electron binding by a rotationally excited dipolar system has been elucidated, and critical dipole moments have been determined for the first four rotational states of the electron-dipole system.

Contrary to results obtained by earlier investigators, the total scattering cross section for charged particles scattering from a finite stationary dipolar system has been shown to be divergent. The contradictions and the gross underestimate in total and momentum transfer cross sections in earlier theoretical treatment of the problem were shown to be due to truncation errors in a divergent series.

7. Interaction of Radiation with Liquids and Solids

The electronic response of solids to electromagnetic radiation has been studied further by measuring the optical properties of Rb and UN in the vacuum

1147996

ultraviolet region of the spectrum and of In and Sn by ellipsometric techniques in the visible region. Soft x-ray emission of the L_{23} core level of Mg in MgO and MgF_2 and the high-energy satellites in Na, Mg, Al, and Si have been investigated. Finally, the attenuation length of low-energy electrons in Al and the plasma energy in Mg have been measured by photoelectric techniques.

8. Physics of Tissue Damage

Comparison of the electron-slowing-down spectrum in a semiconductor and a metal has shown very little difference, suggesting that biological materials may be approximated by low-Z metals for studies of this type. The electron flux has been measured for silicon beta particles slowing down in silicon as well as the Auger cascade electrons from thulium slowing down in ytterbium.

Optical absorption k has been obtained for several organic liquids and silicone pump oils over the energy region from 4.0 to 10.65 eV. These data were obtained using a transmission cell with liquid samples as thin as 500 Å.

9. Electron and Ion Collision Physics

Absolute cross sections for the production of slow electrons (0 to ~1 eV) upon electron impact ionization of He, Ne, and Ar have been measured in the incident electron energy range from 0 to 500 eV. For incident electron energies from 100 to 500 eV the slow electron production cross sections fall off in the same manner as the total ionization cross sections for all of the rare gases. The measured slow electron production cross sections are useful in describing electron-slowing-down spectra in gases.

Negative-ion processes were studied in the boron halides BF_3 and BCl_3 using both electron beam and electron swarm techniques. The thermal energy electron attachment rate for BF_3 was found to be quite small, if not zero, and F^- was found to occur at the anomalously high incident electron energy of 11.5 eV. These studies have been related to the operation of BF_3 in neutron dosimeters.

Electron impact excitation and negative-ion formation have been studied in a series of carbonyl compounds. New electronic states and negative-ion states have been discovered. The energy positions of the negative-ion states are in agreement with the electron withdrawing and donating effects of the various substituents.

Electron attachment and diffusion coefficients have been determined for O_2 in the difficult thermal energy range. This work is the first measurement of electron transport properties of thermal electrons in molecular oxygen. Previous measurements have been obscured by attachment.

Ion products from the collisions of fast cesium atoms with O_2, NO_2, and N_2O have been mass-identified from the reaction threshold to approximately 40 eV in the laboratory system. Accurate measurements of the threshold for ion pair production yield electron affinities of 0.46 ± 0.05, 2.09 ± 0.2, and ~0 ± 0.3 eV for O_2, NO_2, and N_2O, respectively. The experiment will be used to determine greatly needed information on electron affinities of organic molecules.

10. Atomic and Molecular Radiation Physics

A new technique has been established which allows direct determination of electron attachment cross sections as a function of electron energy from high-pressure electron swarm data alone. This technique has been tested and shown to be uniquely suited for electron attachment resonances with cross sections increasing sharply at thermal energies. Results are presented for a number of molecules. The results of a study on dissociative electron attachment to halogenated aliphatic hydrocarbons are presented also, and preliminary data on electron capture by molecules forming "moderately short-lived" negative ions under high-gas-pressure conditions are outlined. Lifetimes τ of long-lived polyatomic negative ions have been measured for a number of organic molecules, and the dependence of τ on electron energy has been accurately determined. The presence of π electrons in organic molecules has been found to enhance the scattering of slow electrons from such systems. Threshold electron excitation spectra for a number of molecules have been studied and revealed new compound negative-ion states. A formalism of quasi-equilibrium theory of unimolecular decomposition based on microscopic reversibility has been developed and applied to unimolecular dissociation of excited ions. Preliminary results of our effort to link existing data on electron attachment in gases with those in the liquid phase are presented. Optical emission spectra from the second excited π-singlet state of six organic molecules in solution have been clearly observed. Photophysical studies of organic liquids and solutions indicate that such emissions from higher π-singlet states of aromatic hydrocarbons are not uncommon.

1147997

11. Graduate Education and Vocational Training

Six AEC Fellows were trained at ORNL in applied health physics. Nineteen students were enrolled in the health physics courses taught by the Division at Vanderbilt University and The University of Tennessee. Seventeen schools were visited by staff members to discuss health physics research and educational activities. Twenty-one students conducted thesis research in the Division leading to the M.S. or Ph.D. degree. A great deal of assistance was given to ORAU in conducting numerous USAEC-sponsored programs.

PART III. RADIATION DOSIMETRY RESEARCH

12. Dosimetry for Human Exposures and Radiobiology

The medical applications of ^{252}Cf sources and the special dosimetric problems encountered by medical physicists continue to be of interest in the program of calculating distributions of dose with depth in a tissue-equivalent phantom. During this report period, emphasis has been placed on calculations for gamma rays from the source as well as secondary gammas. An extensive evaluation and analysis of previous calculations has been completed. This analysis was intended to reveal the reactions of importance for given neutron energies, as well as the percentage of total dose for each reaction. Extensive measurements of neutron and gamma-ray dose as a function of depth in a tissue-equivalent phantom have been completed for radiation fields from the HPRR and from a 14-MeV neutron generator. Liaison with the Atomic Bomb Casualty Commission has continued in an effort to assign dose to the 1100 remaining individuals for whom shielding histories exist. Studies related to the determination of dose for persons exposed in reinforced concrete buildings in Japan have been intensified.

13. Applied Dosimetry Research

Major emphasis in the solid state dosimetry program this year was placed on the role of activators in TSEE detectors, sensitizing ceramic BeO detectors, identifying damage mechanisms and trapping centers, and improving chambers for reading out the exoelectrons. It was found that ceramic BeO, Thermalox 995, is most sensitive after a heat treatment at 1400°C for several hours. Silicon, which is the major impurity in 995 BeO, was found to be the activator responsible for the 325°C peak in the exoelectron distribution. It is believed that Si^{4+} in place of Be^{2+} acts as an electron trap because of its excess positive charge with respect to the normal lattice sites. The effect of other parameters such as Li^{+} activation and deuteron bombardment on the detectors and their dosimetric implications were also studied. Experiments on the properties of phosphors such as $CaSO_4$:Dy, $CaSO_4$:Tm, CaF_2:Dy, and LiF:Mg,Ti as thermoluminescence dosimeters were performed in a tropical environment. These studies were directed at determining sensitivity of the detectors and signal fading under various conditions. Nuclear track etching studies were continued with emphasis given to the application of track detectors to personnel dosimetry, in particular to the use of small quantities of ^{237}Np.

14. Interaction of Charged Particles with Matter

A major effort is being made to determine the energy pathways involved when charged particles interact with gases. A six-in-one experiment is being conducted using the ORNL 3-MV Van de Graaff: radiation intensities as a function of wavelength and pressure for pure noble gases, quenching of electromagnetic radiation by additive gases, *W* values for the pure gases, *W* values for the gas mixture (Jesse effects), lifetimes of continuous and resonance radiations, and absolute intensities of radiation into the vacuum ultraviolet region. These studies have led to the formation of graphic models for the emission processes from helium and argon molecules. The emission model for argon appears to explain the fact that quenching of the 1250-Å emission involves a kinetic scheme which is more complicated than the Jesse effect. Separate studies of the resolved radiation at 1048 Å, the 1100-Å continuum, and the 1250-Å continuum should provide an interpretation of the detailed ways in which quenching collisions intercept the energy flow.

15. Spectrometry Research and Development

Much of the research in spectrometry has been directed toward the purification of organic scintillators. For *para*-quaterphenyl purified by zone refining, most of the impurities which limit light output were removed. This purified material has about the same emission for gammas as anthracene. *Para*-sexiphenyl purification is accomplished through a process of recrystallization. Preliminary measurements made on the single crystals of *para*-sexiphenyl reveal that the optical index of refraction lies above 1.64, that the crystals are completely transparent to visible light, and that the fluorescence spectrum indicated a single large

1147998

peak at 450 nm. It is expected that for better purification the peak should shift to near the theoretical maximum of 430 nm. In the area of instrumentation, a voltage-to-frequency converter was built to digitize the output of an electrometer so that the digital signal could be summed with a scaler. Integrated circuits are used for amplification of input voltages, as a variable current source for the relaxation oscillator, and for output pulse shaping. It was designed to operate in an NIM power unit.

16. HPRR and Accelerator Operations

The HPRR was operated routinely and without fault, and no change has been noted in any of the systems or core components. In May 1971, the eighth intercomparison of nuclear accident dosimetry systems was conducted. This study was cosponsored by the International Atomic Energy Agency, and representatives from 11 foreign countries participated. The HPRR was used to provide three radiation fields to simulate nuclear accidents with three different neutron spectra. Studies of the energy pathways involved when charged particles interact with matter were done using the 3-MV Van de Graaff. The DOSAR Low-Energy Accelerator was used in support of depth-dose studies in tissue-equivalent phantoms. A new target using a Pd-Ag foil to pass ^{3}H from a reservoir to the target area has been tested successfully. This target was operated for 10 hr at an average yield of 3×10^{10} neutrons/mA-sec.

PART IV. INTERNAL DOSIMETRY

The specific absorbed fraction of photon energy is known to be much greater for younger children than for adults; hence, the dose per unit activity to a target organ from a photon emitter in a source organ is correspondingly greater for individuals of younger ages. The fact that organs in the young are closer to each other than in the adult and the inverse square law for variation of dose with distance are the bases for the expected increase of dose, but quantitative data correlating absorption factors with age have been lacking. The data in the first study reported by the Internal Dose Estimation Section are a first step toward filling this gap. While the data are preliminary, they demonstrate the expected increase of dose at younger ages as well as a means of supplying the dose estimates for various age groups. Such estimates are of great importance in nuclear medicine and in obtaining reliable estimates of dose for population exposure.

The report on "Dose to a Developing Fetus from a Gamma Emitter in the Bladder" is a first effort to fill another gap in the dosimetry of internally deposited radionuclides. When gamma emitters are present in an organ of the body, the fetus will be irradiated to some extent, and the bladder is of particular importance because it lies close to the fetus and also because many radionuclides are excreted through the bladder. The results reported here make it possible to obtain a realistic estimate of dose for this case. The study has obvious application in nuclear medicine as well as for estimating population exposure.

Realistic estimates of absorbed fractions of energy have been obtained using the Monte Carlo technique and have been published in MIRD Pamphlet No. 5. However, there are many cases where the statistical uncertainty of these estimates is so great that a blank was left in the table. The gonads represent a case of particular interest where estimates are lacking. In the study on "Specific Absorbed Fractions for Internal Emitters," the Monte Carlo estimates of MIRD Pamphlet No. 5 are compared with estimates calculated for an infinite homogeneous medium of tissue. The results suggest that estimates obtained in this way do not differ by more than a factor of 2 from those obtained in the finite nonhomogeneous phantom and, on the average, are not more than 20 to 30% in error. Since errors of this magnitude will frequently be found due to individual characteristics, the use of specific absorbed fractions calculated for the infinite medium seems appropriate for those cases where the more precise Monte Carlo estimates are not available.

The estimation of dose to the skin and subcutaneous tissues from an atmosphere containing a radioactive aerosol is a problem of considerable importance for purposes of estimation of dose to the population living near a nuclear plant. In the past, only an estimate of "surface dose" has been used, and this did not adequately represent the dose to subcutaneous tissues such as testes, lenses of the eyes, etc. Using data of Berger (MIRD Pamphlet No. 8) on dose at a distance from a point source, a computer code has been developed for estimating depth dose in tissue from a uniform "cloud" of radioactive material present in the air surrounding the body. The estimates can be obtained either for monoenergetic electrons or for beta rays emitted by the radionuclide.

Data from the literature have been analyzed to obtain practical models for metabolism of ^{232}Th. The data as published only provide an indication of the various "pools" or compartments and some indications of exchange rates between these compartments. From these indications, metabolic models are obtained which can then be tested with other data, particularly that relating to the naturally occurring isotope.

1147999

Part III. Radiation Dosimetry Research

J. A. Auxier

12. Dosimetry for Human Exposures and Radiobiology

J. W. Poston

J. A. Auxier
J. S. Cheka
W. L. Chen[1]
W. F. Fox
H. H. Hubbell, Jr.
J. E. Jackson
T. D. Jones
E. M. Robinson
W. H. Shinpaugh
W. S. Snyder
M. Sohrabi[1]

JAPANESE DOSIMETRY PROGRAM

Heavy Shielding Research

The cooperative program with the Atomic Bomb Casualty Commission (ABCC) in Japan has been concerned the past year with assisting them in computing radiation doses to the last 1100 or so of the survivors for whom shielding histories exist. Dose values had not previously been assigned to these cases. They constitute principally persons in heavy shielding situations, such as reinforced concrete buildings. The liaison representative from ORNL worked out and checked at ABCC a simplification of the procedure for evaluating the shielding effect of concrete walls having variable thickness, because of built-in posts, etc. The average concrete thickness is used in such cases, and calculations show a maximum error introduced in the final dose of only 2 to 3%. This simplification will save considerable time.

In order to refine the techniques and input data for such heavy shielding calculations, a large collimator which had been used in the Nevada Test Site at Operations BREN and HENRE was brought to Oak Ridge and set up on the roof of Building 7710. It will be used to measure the angular distribution of the scattered neutron and gamma radiations reaching the building from the Health Physics Research Reactor (HPRR) on the other side of a hill. From these data the attenuation of the doses by the concrete building and the doses inside will be calculated to check those measured experimentally. It is expected that this work will permit refinement of the shielding calculation techniques used at ABCC and of civil defense calculations.

In Utero Exposure

For the correlation of specific biological responses such as thyroid carcinoma and effects of radiation on those who were in utero survivors in Hiroshima and Nagasaki, a complete description of the internal dose distributions is desirable. In 1970, results were presented for the contribution to dose from (1) the neutron field and from (2) photons produced by neutron interactions inside the phantom, for circular cylinders having heights of 60 cm and radii of 6, 12, and 15 cm, corresponding to the neck and adult human torsi. Dose data for the same phantoms are given here

1. Alien guest.

1148000

for gamma rays produced exterior to the phantoms. The photon field, external to the phantoms, was assumed to be isotropic, and its energy spectral distribution[2] is shown in Fig. 12.1. The corresponding dose distributions in the three phantoms are shown in Fig. 12.2. From these distributions and those presented in 1970, it appears that fetal size and directional orientation of the mother are relatively unimportant (except for an extremely late stage of fetal development) because the dose distribution curves are relatively flat across the fetus, ensuring a nearly constant level of exposure. The thyroid gland is not centered in a sagittal plane through the neck, and consequently, unlike the fetus, is not uniformly exposed. Orientation of the survivor is still not very important because contributions to the radiation field are nearly symmetrical with respect to direction.

2. E. A. Straker and M. L. Gritzner, *Neutron and Secondary Gamma-Ray Transport in Infinite Homogeneous Air*, ORNL-4464 (December 1969).

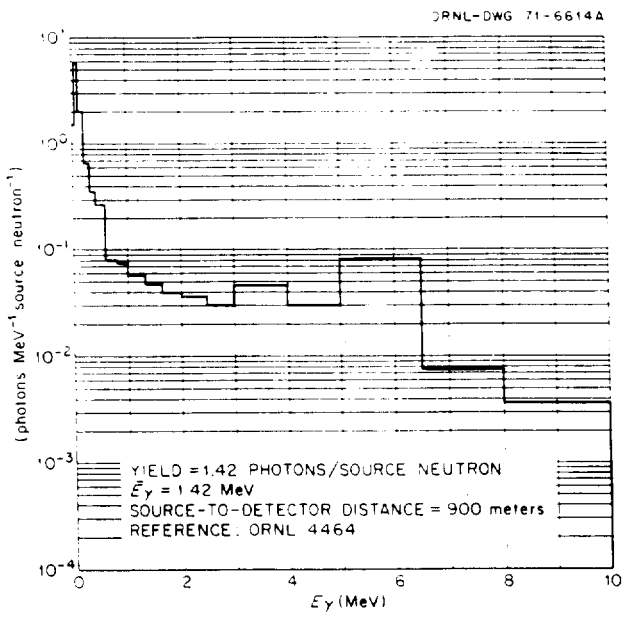

Fig. 12.1. $4\pi R^2$ photon energy spectrum produced by a distant nuclear explosion in an infinite air medium.

CALCULATIONS OF DOSE AND LET DISTRIBUTIONS FOR NEUTRONS AND GAMMA RAYS

Californium-252 – Therapeutic Sources

Distributions of dose equivalent (DE), linear energy transfer (LET), absorbed dose from neutron-produced photons, and absorbed dose from neutron-produced recoil ions from therapeutic implanted and external sources of ^{252}Cf were presented in 1970. The data in Table 12.1 were computed from Barker (1969)[3] and were used in a Monte Carlo sampling technique to choose the source energies of the photons. For internally located sources of ^{252}Cf, the contributions to dose and LET from photons emitted by the spontaneous fission of ^{252}Cf become quite significant. Figure 12.3 shows dose from electrons produced by photons emitted by the spontaneous fission of ^{252}Cf as

3. J. J. Barker (ed.), *Californium-252*, CONF-681032 (1969).

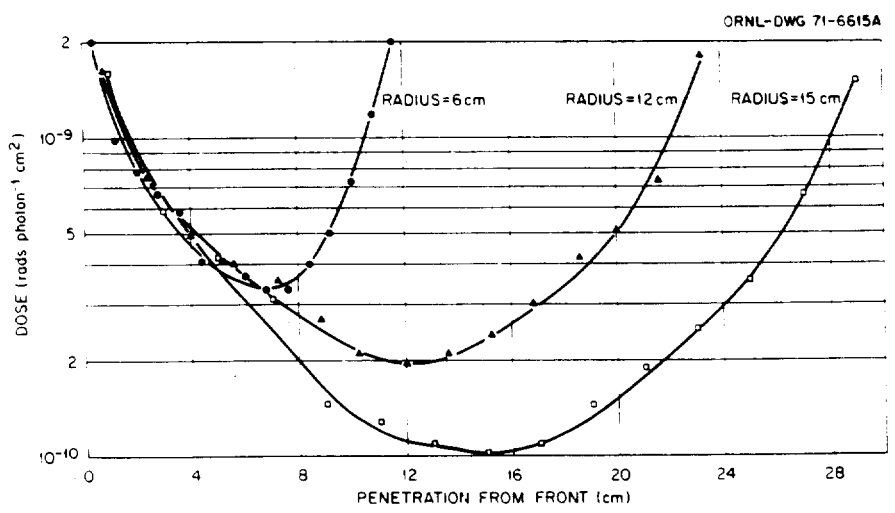

Fig. 12.2. Dose from the photon field external to the phantom.

1148001

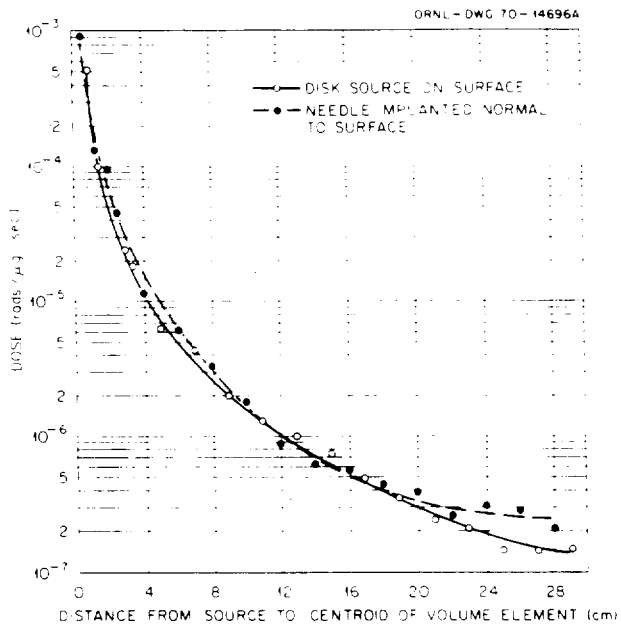

Fig. 12.3. Dose from fission-produced gamma rays as a function of distance from the centroid of a ^{252}Cf source.

Table 12.1. Probability of production of a photon having energy E from the spontaneous fission of ^{252}Cf

Energy (MeV)	Probability
0 to 0.5	0.3479
0.5 to 1.0	0.4312
1.0 to 1.5	0.1286
1.5 to 2.0	0.0582
2.0 to 2.5	0.0166
2.5 to 3.0	0.0083
3.0 to 3.5	0.0042
3.5 to 4.0	0.0022
4.0 to 4.5	0.0012
4.5 to 5.0	0.0006
5.0 to 5.5	0.0003
5.5 to 6.0	0.00014
6.0 to 6.5	0.00008
Total	0.9986

a function of distance from the source to the centroid of the volume element of interest. For internally located therapeutic sources of ^{252}Cf, the contribution from these photons is extremely important and must be taken into account. Earlier work indicated that there is little, if any, air-tissue interface effect on dose for normally oriented needle-implanted sources; however, several therapists recently became concerned about the magnitude of the change in dose to a tumorous region for an implanted source lying parallel to and within a distance of about 0.5 cm of the air-tissue interface.

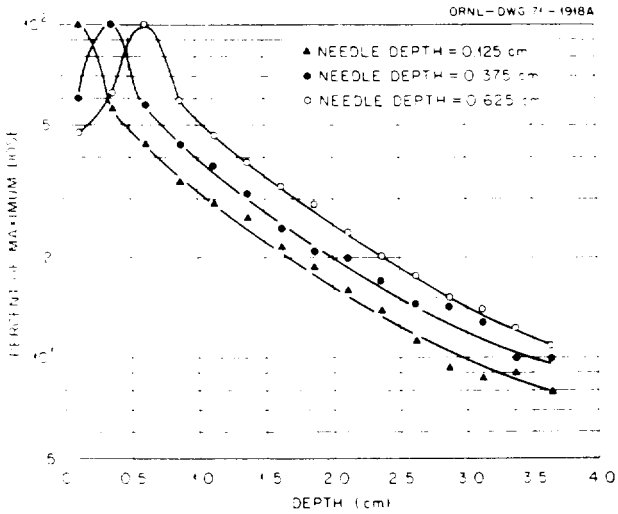

Fig. 12.4. Percent of maximum dose vs depth for ^{252}Cf needles implanted parallel to the surface.

There has even been speculation that the dose to a tumorous region may be decreased by from 4 to 25% relative to the infinite medium geometry.

Figure 12.4 shows the interface effect on dose in a 30-cm cube of tissue-equivalent medium for ^{252}Cf needles, implanted parallel to the surface at depths of 0.125, 0.375, and 0.625 cm. Coefficients of variation for the maximum or peak values (in units of dose) of the three curves shown in Fig. 12.4 were less than 0.05, while the spread of the three maximum values (in units of dose) was only 0.08, and no explainable systematic deviation was apparent. Thus, from these calculations the nearness of an air-tissue interface appears to have no significant effect on the dose from implanted ^{252}Cf needles.

Broad-Beam Neutron Exposures

A recurring problem in dosimetry is the comparison of calculational results to experimental ones and the determination of how closely and over what energy range they should agree. In many exposure situations, one can simply measure dose from either the hydrogen elastic or the $^{1}H(n,\gamma)^{2}H$ reactions and account for about 90% of the dose, but one has to know which reactions to consider for a specified geometry and source energy and under what conditions it is desirable to consider both reactions. Usually these two reactions, either individually or together, depending upon phantom geometry and source energy, account for at least 90% of the dose. At energies below about 2.5 MeV the $^{14}N(n,p)^{14}C^{*}$ reactions account for most of the

1148002

remainder, but for higher energies the remainder is usually broken up among several different reactions.

The whole-body contributions to dose from $^{1}H(n,\gamma)^{2}H$, $^{14}N(n,p)^{14}C^{*}$, and hydrogen elastic reactions in cylindrical tissue-equivalent phantoms corresponding in size to a rat, rabbit, and man are given in Fig. 12.5. For low source energies (rat, $E \lesssim 1$ keV, rabbit, $E \lesssim 10$ keV; man, $E \lesssim 100$ keV), most of the contribution to dose comes from the $^{1}H(n,\gamma)^{2}H$ reactions with nearly all of the remainder from the $^{14}N(n,p)^{14}C^{*}$ reactions. Structure characteristic of the curves for fraction of dose from $^{1}H(n,\gamma)^{2}H$ appears to occur at an increase in energy by about an order of magnitude for the comparison of rat to rabbit and rabbit to man. Likewise, there appears to be a similar effect for the hydrogen elastic reactions associated with a decrease in energy. Sections of the curves from the $^{1}H(n,\gamma)^{2}H$ and the $^{14}N(n,p)^{14}C^{*}$ reactions have been plotted on the distributions for the hydrogen elastic reactions in order to illustrate which reactions need to be considered for a given source energy and phantom geometry. The fraction of total dose from $^{1}H(n,\gamma)^{2}H$ reactions as a function of penetration depth inside the man phantom for various source energies is described in Fig. 12.6. Similar curves were computed for the rabbit and rat phantoms. One must be careful in the use of a single reaction for the description of total dose because of situations like the 100-keV neutron beam incident on the man-sized phantom shown in Fig. 12.6. For this case the $^{1}H(n,\gamma)^{2}H$ reactions contribute about 86% of the total dose to the phantom; however, at a penetration depth of 1 cm, it contributes less than 30% of the total local dose. Figure 12.5 indicates that the hydrogen elastic reaction is most important for a wide

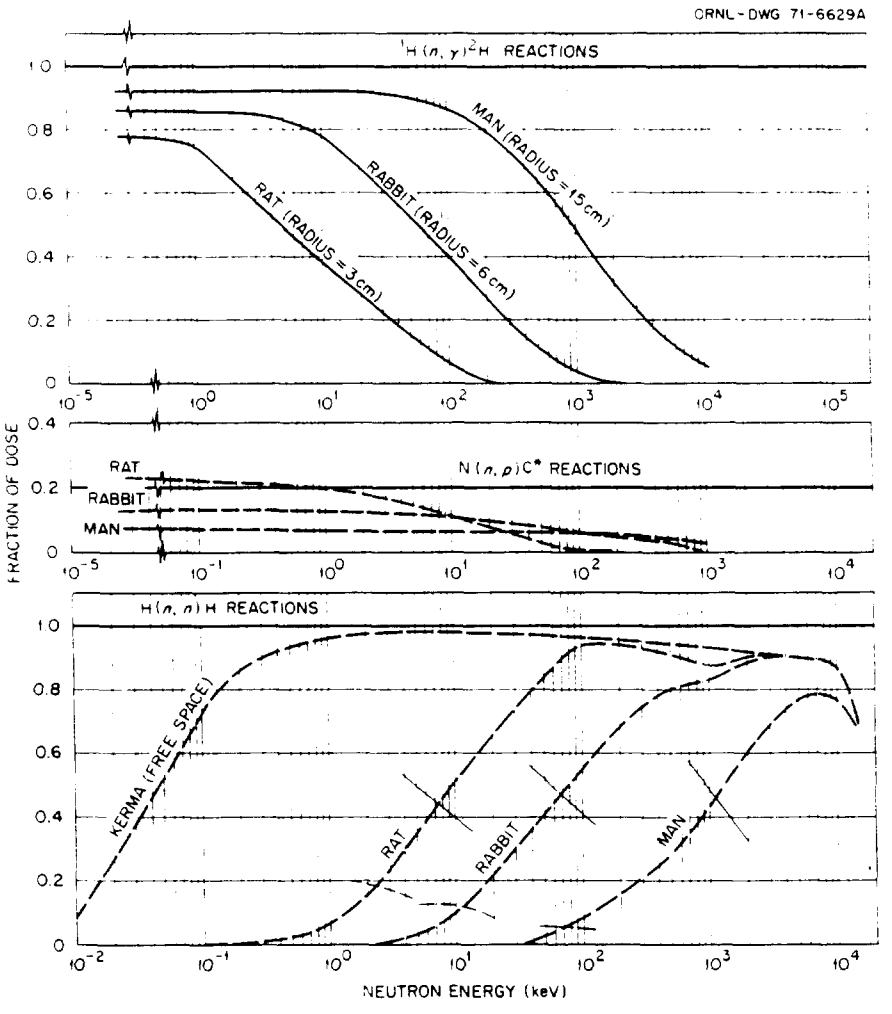

Fig. 12.5. Contributions to dose from important reactions in standard soft tissue from a broad parallel beam of monoenergetic neutrons.

1148003

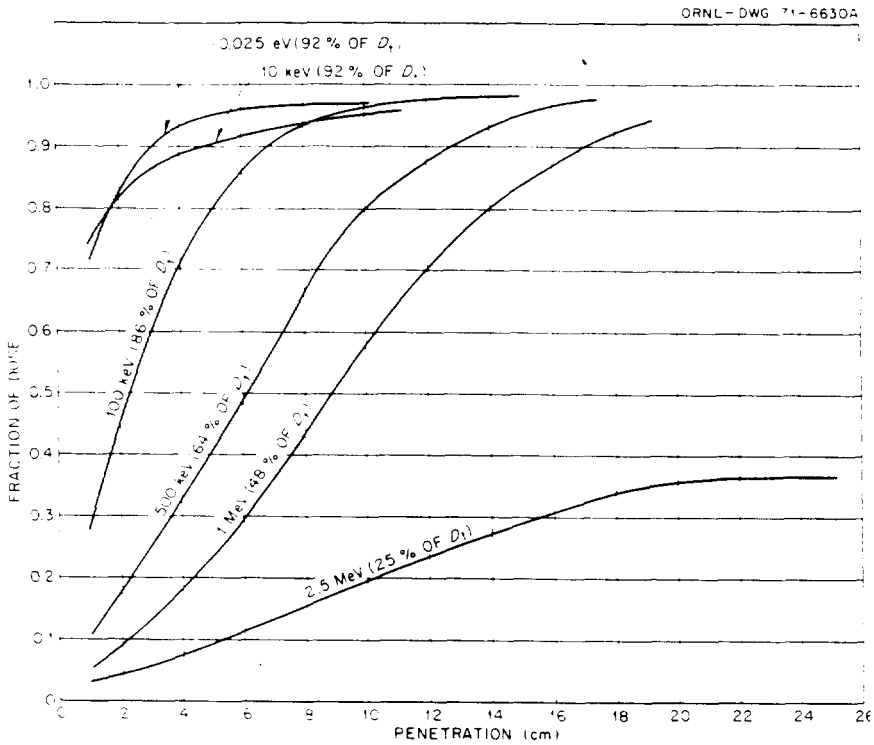

Fig. 12.6. Distribution of dose from $^{1}H(n,\gamma)^{2}H$ reactions in a man-sized phantom exposed to a broad parallel beam of monoenergetic neutrons.

range of source energies. Figure 12.7 shows dose as a function of penetration depth in a man-sized cylindrical phantom, exposed to a broad parallel beam of neutrons, having an energy spectral distribution equal to that of the HPRR. Table 12.2 expresses the distribution of the energy of neutrons produced by the HPRR. Column 3 is the probability that a particular neutron is in that specific energy range, and column 4 gives the probability that a given neutron has an energy inside of or greater than that specific energy range. Column 4 shows that about 89% of the neutrons emitted from the HPRR assembly have energies greater than about 160 keV. An energy cutoff of 160 keV was used, and dose from hydrogen elastic reactions only was recorded as a function of depth. This was done because of the response of the recoil proton proportional counter, used in measuring neutron dose, which has such an energy cutoff. It appears that 90% of the spectrum on the high-energy end of the distribution contributes 90% of the total dose from recoil ions, and the distribution does not significantly change from the distribution of the total dose. The change in the distribution of the fraction of dose per unit LET as a function of LET is more notable. The characteristic shape is basically the

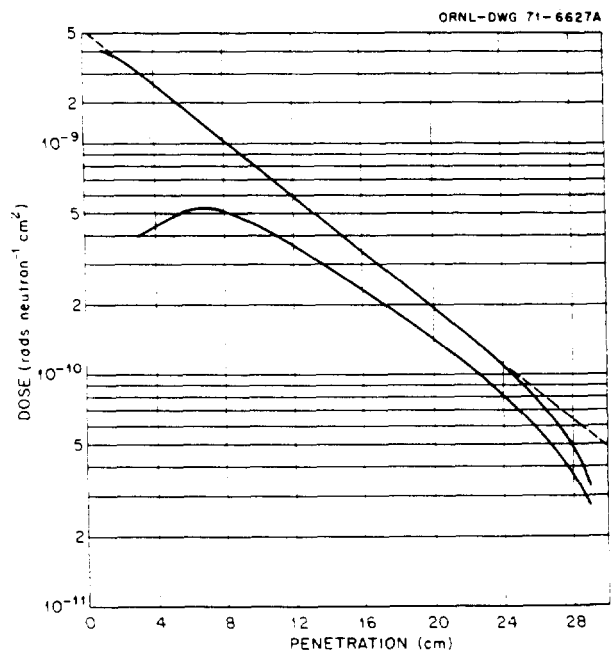

Fig. 12.7. Dose in a man-sized cylindrical phantom exposed to a broad parallel beam of neutrons having an energy spectral distribution equal to that of the HPRR.

1148004

Table 12.2. Distribution of the energy of neutrons produced by the HPRR

Group	Energy range ($E_U - E_L$)	$P(E_L < E < E_U)$	$P(E > E_L)$
1	14.92–3.01 MeV	0.0996	0.0996
2	3.01–1.50 MeV	0.179	0.279
3	1.50–0.91 MeV	0.157	0.436
4	0.91–0.41 MeV	0.268	0.704
5	0.41–0.11 MeV	0.188	0.892
6	110–87 keV	0.0123	0.904
7	87–67 keV	0.00907	0.913
8	67–52 keV	0.00679	0.920
9	52–41 keV	0.00539	0.925
10	41–32 keV	0.00438	0.930
11	32–25 keV	0.00372	0.934
12	25–19 keV	0.00321	0.937
13	19–15 keV	0.00285	0.940
14	15–7.1 keV	0.00711	0.947
15	7.1–3.4 keV	0.00596	0.953
16	3.4–1.2 keV	0.00669	0.959
17	1200–580 eV	0.00433	0.964
18	580–214 eV	0.00488	0.969
19	214–101 eV	0.00300	0.972
20	101–48 eV	0.00309	0.975
21	48–29 eV	0.00185	0.976
22	29–18 eV	0.00176	0.978
23	18–11 eV	0.00167	0.980
24	11–5.0 eV	0.00234	0.982
25	5.0–3.1 eV	0.00145	0.984
26	3.1–1.6 eV	0.00185	0.986
27	1.6–1.0 eV	0.00118	0.987
28	1.0–0.66 eV	0.00107	0.988
29	0.66–0.45 eV	0.000886	0.989
30	0.45–0.10 eV	0.00760	0.996
31	Thermal	0.00470	1.000

same, except that the high end of the LET distribution is lost. In addition to this, there is a shift of dose from both high and low LET to the 10-to-40-keV/μ region. For a 14-MeV neutron source and an energy cutoff of 160 keV, Fig. 12.8 shows that dose from hydrogen elastic reactions consists of about 65% of the total and is distributed more uniformly through the phantom than is total dose. Thus under these conditions a dosimeter that is only sensitive to proton recoils should not agree closely with curves for total dose. Figure 12.9 shows that there is also a significant shift toward low LET for the distribution of dose as a function of LET, and LET measurements should take this fact into account.

Photon Exposures

The heterogeneous phantom discussed in ORNL-4584 (ref. 4) was assumed to be unilaterally irradiated by a

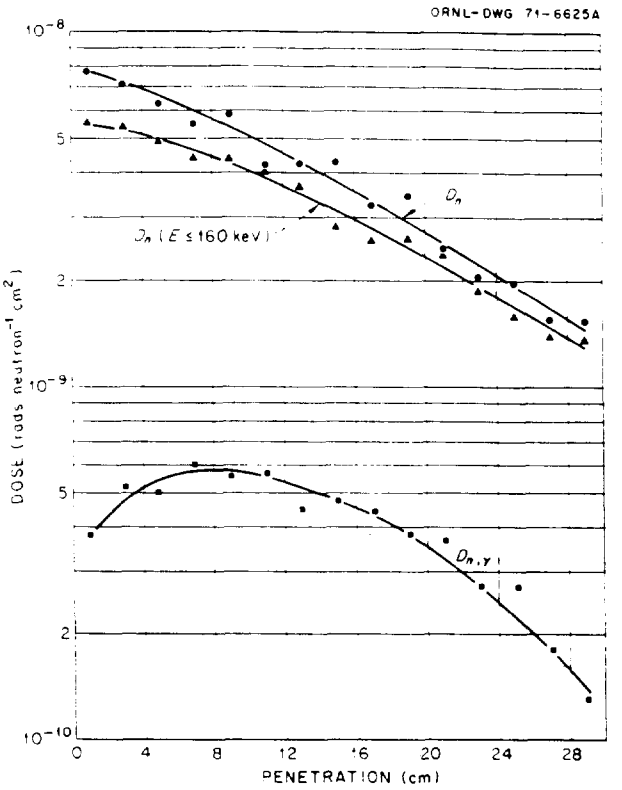

Fig. 12.8. Dose in a man-sized cylindrical phantom exposed to a broad parallel beam of 14-MeV neutrons.

parallel beam of monoenergetic photons limited to incidence on the torso. It contained most of the important organs, and the skeletal approximation included both red and yellow marrow. Photons which entered the phantom were permitted to scatter into the legs and head region and even scatter back into the torso. The extent of the photon beam was determined by the projected area of the torso. Photon source energies were 50, 100, 250, and 660 keV, and 1.25, 3, 6, and 10 MeV.

Since the lower abdomen of the phantom is nearly free of bone, except for a small section of the pelvis which protrudes into tier 1, the results for these irradiations closely approach the homogeneous case and the curves for anterior irradiation. For anterior exposure the nearness of the lungs ($\rho \doteq 0.3$) and the effect of averaging dose to part of the spine into some of the volume elements may be seen in Fig. 12.10. Data for tiers 1, 2, and 3 do not show much "bone effect" for photon energies above 250 keV. At higher energies the "effect" appears to be lost due to (1) the longer mean

4. *Health Phys. Div. Annu. Progr. Rep. July 31, 1970*, ORNL-4584, p. 200.

1148005

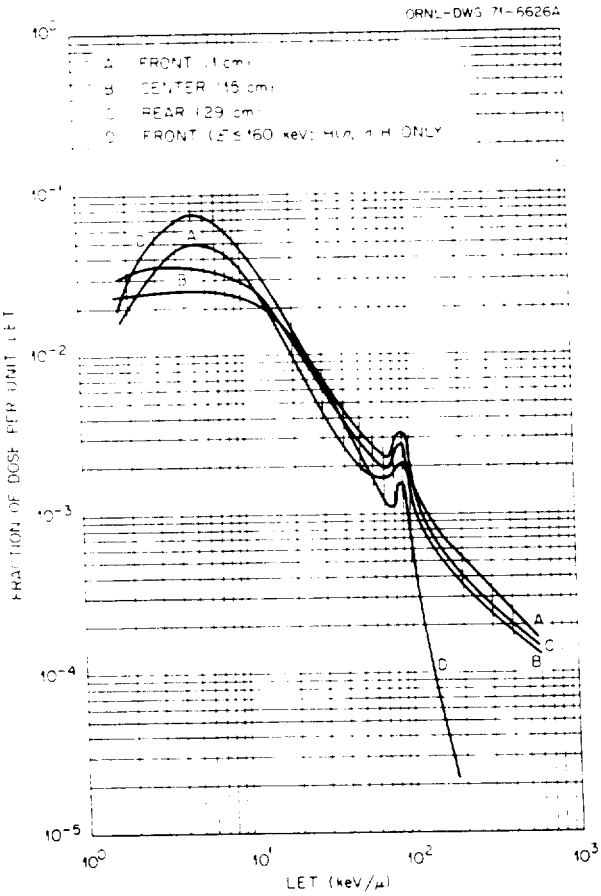

Fig. 12.9. Fraction of dose per unit LET as a function of LET from 14-MeV neutrons.

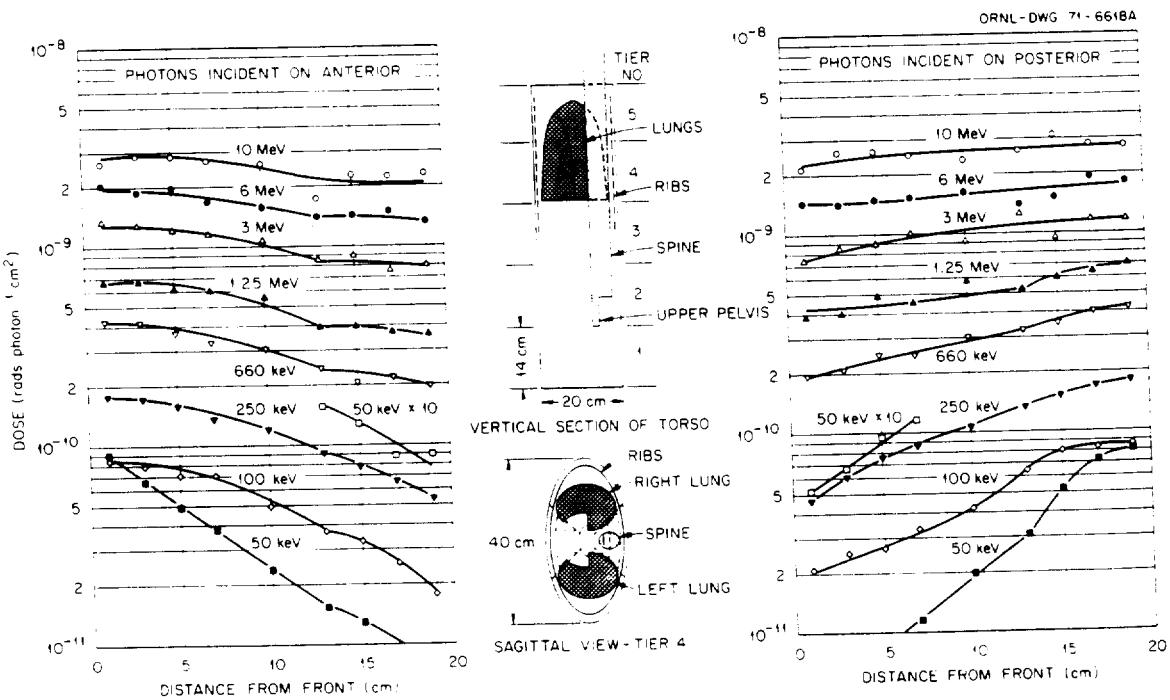

Fig. 12.10. Dose from a broad parallel beam of monoenergetic photons incident unilaterally on the chest of a standard 70-kg human.

1148006

collision path length which is inversely proportional to the linear absorption coefficient and to (2) an increase in the variance of the dose contribution to a given volume element.

Tables 12.3, 12.4, and 12.5 give doses to some organs of the human body for anterior, posterior, and left-side irradiation, respectively. Cases where doses have coefficients of variation larger than 0.20 should be checked against the depth-dose data in Figs. 12.10 and 12.11 before any use is attempted. The variations of dose to most organs generally tend to be linear with photon energy; however, the volume of the ovaries is only 8.8 cm^3, and statistical parameters are large enough that under no condition should the data from Tables 12.3, 12.4, and 12.5 be used without first checking them against plotted depth-dose data.

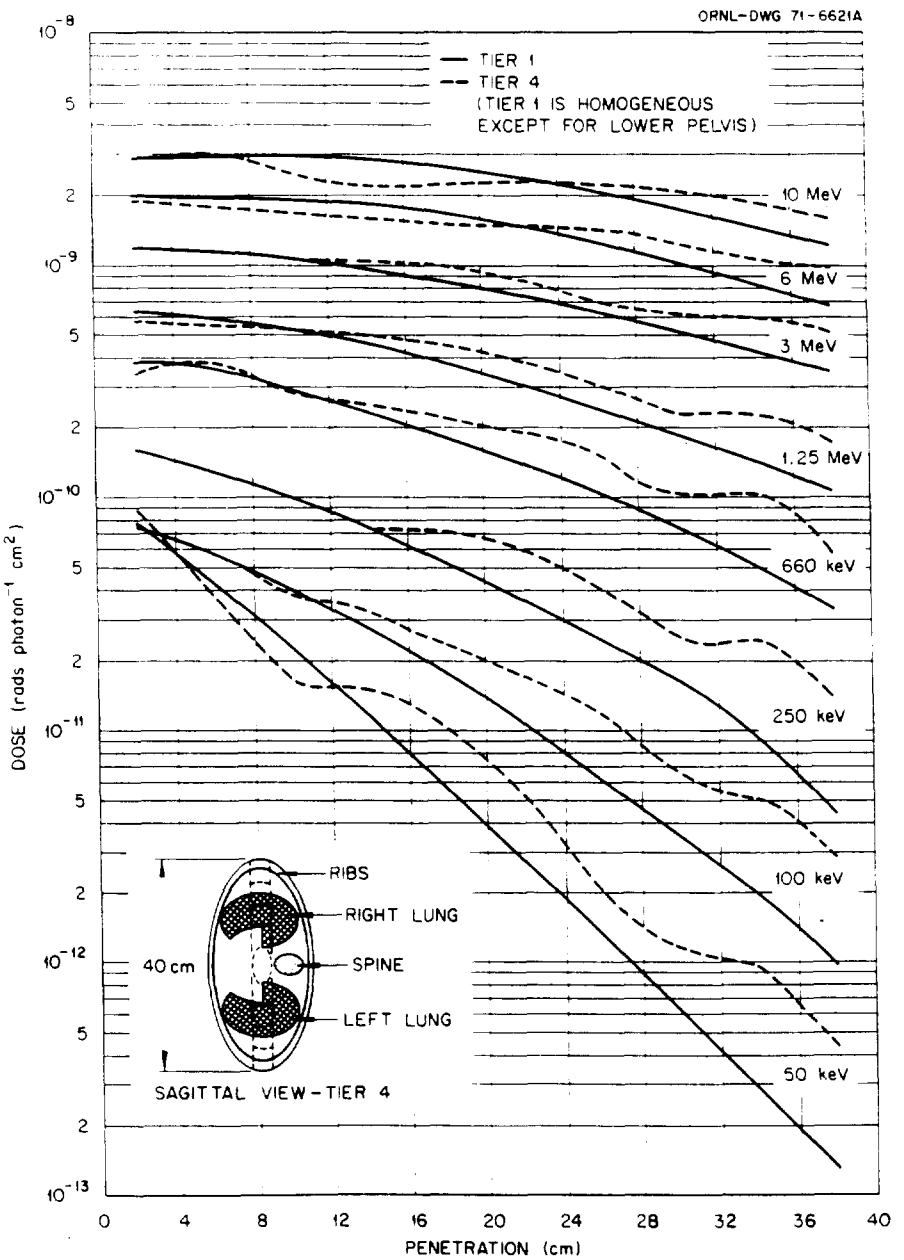

Fig. 12.11. Dose from a broad parallel beam of monoenergetic photons incident unilaterally on the left side of a standard 70-kg human.

1148007

Table 12.3. Dose to some organs of the human body irradiated by a broad parallel beam of monoenergetic photons incident on the anterior of the torso

Organ	50 kev		100 kev		250 kev		660 kev		1.25 Mev		3 Mev		6 Mev		10 Mev	
	Dose (rads y^{-1} cm^2)	C of V (%)	Dose (rads y^{-1} cm^2)	C of V (%)	Dose (rads y^{-1} cm^2)	C of V (%)	Dose (rads y^{-1} cm^2)	C of V (%)	Dose (rads y^{-1} cm^2)	C of V (%)	Dose (rads y^{-1} cm^2)	C of V (%)	Dose (rads y^{-1} cm^2)	C of V (%)	Dose (rads y^{-1} cm^2)	C of V (%)
1 Adrenals	6.94-12	34	1.55-11	21	4.16-11	25	6.20-11	29	4.87-10	35	6.31-10	35	1.47-9	38	1.66-9	52
2 Bladder	5.19-11	7	6.90-11	7	1.38-10	10	4.38-10	12	7.62-10	17	1.17-9	19	1.66-9	23	3.70-9	21
3 Contents	5.18-11	4	6.78-11	4	1.42-10	5	3.41-10	6	6.52-10	9	1.14-9	9	1.87-9	10	2.81-9	11
4 Clavicles	9.67-11	6	6.93-11	7	1.20-10	9	2.55-10	12	4.82-10	17	8.76-10	16	1.14-9	21	2.15-9	21
5 GI stomach	5.37-11	4	7.60-11	4	1.67-10	5	4.10-10	6	5.80-10	11	1.01-9	11	1.45-9	13	2.86-9	13
6 GI ULI	3.74-11	4	5.93-11	4	1.43-10	5	3.06-10	6	4.98-10	10	9.72-10	9	1.57-9	11	2.88-9	11
7 GI LLI	2.60-11	5	4.62-11	5	1.26-10	6	3.20-10	7	5.15-10	11	1.02-9	10	1.74-9	12	2.72-9	13
8 GI contents	5.44-11	2	8.72-11	2	2.03-10	2	4.98-10	3	8.43-10	4	1.59-9	4	2.46-9	5	3.88-9	5
9 GI small int & contents	3.10-11	2	5.63-11	2	1.34-10	2	3.44-10	3	5.46-10	4	9.99-10	4	1.76-9	5	2.66-9	5
10 Heart	4.26-11	3	6.46-11	3	1.45-10	3	3.54-10	4	5.46-10	6	1.08-9	5	1.79-9	6	2.68-9	7
11 Kidney left	8.58-12	11	2.40-11	8	6.46-11	8	2.38-10	9	3.08-10	14	8.55-10	12	1.99-9	12	2.47-9	14
12 Kidney right	8.28-12	10	2.40-11	8	7.54-11	8	2.08-10	9	4.68-10	12	8.46-10	12	1.19-9	15	2.10-9	15
13 Liver	4.13-11	2	6.14-11	2	1.46-10	2	3.46-10	2	6.08-10	3	1.07-9	3	1.79-9	4	2.68-9	4
14 Lung left	2.95-11	3	4.74-11	3	1.29-10	3	3.33-10	4	5.60-10	6	1.14-9	6	1.43-9	7	2.26-9	8
15 Lung right	2.93-11	3	4.78-11	3	1.21-10	3	3.20-10	4	5.54-10	6	1.03-9	6	1.43-9	5	2.40-9	8
16 Ovaries	1.12-11	33	4.21-11	25	1.22-10	29	1.72-10	32	5.43-11	59	6.00-10	63	1.44-9	55	1.04-9	44
17 Pancreas	2.49-11	9	4.88-11	8	1.18-10	9	3.07-10	10	2.91-10	21	1.36-9	15	1.90-9	18	2.27-9	22
18 Pelvis	2.78-11	3	4.92-11	3	8.93-11	3	2.29-10	4	4.03-10	5	8.08-10	5	1.49-9	5	2.22-9	6
19 Ribs	8.26-11	2	7.42-11	2	1.11-10	2	2.89-10	3	4.90-10	5	8.81-10	4	1.55-9	5	2.34-9	5
20 Scapulae	1.97-11	6	3.25-11	5	6.74-11	6	1.96-10	7	3.95-10	9	7.90-10	9	1.46-9	10	2.03-9	11
21 Spine	1.05-11	4	3.02-11	3	5.88-11	3	1.64-10	3	2.88-10	5	6.65-10	4	1.07-9	5	1.81-9	5
22 Skeleton	2.41-11	1	2.79-11	1	4.98-11	1	1.26-10	1	2.14-10	2	4.18-10	2	7.02-10	2	1.08-9	2
23 Skin trunk	3.90-11	1	4.41-11	2	1.19-10	2	3.18-10	2	5.29-10	4	1.05-9	3	1.75-9	4	2.72-9	4
24 Spleen	1.87-11	7	3.46-11	6	8.92-11	7	2.55-10	8	6.78-10	9	9.43-10	10	1.68-9	12	3.02-9	12
25 Thymus	5.07-11	10	8.70-11	9	2.02-10	11	4.21-10	16	4.70-10	25	1.00-9	25	2.13-9	27	3.19-9	30
26 Trunk average	3.61-11	0.2	5.08-11	0.3	1.19-10	0.3	3.12-10	0.5	5.43-10	0.7	1.06-9	0.7	1.73-9	0.8	2.58-9	0
27 Uterus	2.17-11	9	3.91-11	9	9.84-11	10	2.13-10	14	3.86-10	20	7.61-10	19	1.14-9	28	2.28-9	20

Table 12.4. Dose to some organs of the human body irradiated by a broad parallel beam of monoenergetic photons incident on the left side of the torso

Organ	50 kev		100 kev		250 kev		660 kev		1.25 Mev		3 Mev		6 Mev		10 Mev	
	Dose (rads y^{-1} cm^2)	C of V (%)	Dose (rads y^{-1} cm^2)	C of V (%)	Dose (rads y^{-1} cm^2)	C of V (%)	Dose (rads y^{-1} cm^2)	C of V (%)	Dose (rads y^{-1} cm^2)	C of V (%)	Dose (rads y^{-1} cm^2)	C of V (%)	Dose (rads y^{-1} cm^2)	C of V (%)	Dose (rads y^{-1} cm^2)	C of V (%)
1 Adrenals	6.75-12	23	2.38-11	15	6.77-11	16	1.99-10	20	4.62-10	20	9.58-10	24	3.66-9	29	2.06-9	33
2 Bladder	6.55-12	12	1.44-11	10	4.74-11	11	2.08-10	11	3.52-10	13	9.99-10	13	1.23-9	18	1.83-9	19
3 Contents	4.91-12	9	1.63-11	6	4.85-11	6	1.70-10	6	3.28-10	7	7.35-10	7	1.36-9	9	2.22-9	9
4 Clavicles	2.40-11	7	2.28-11	8	4.36-11	10	1.21-10	11	2.49-10	12	6.51-10	13	1.11-9	15	1.43-9	17
5 GI stomach	2.13-11	4	4.12-11	4	1.10-10	4	2.81-10	5	5.21-10	6	1.01-9	8	1.16-9	10	2.63-9	9
6 GI ULI	4.70-12	7	1.24-11	6	3.76-11	6	1.27-10	6	2.70-10	7	5.46-10	8	1.15-9	9	1.88-9	9
7 GI LLI	7.21-12	6	2.32-11	5	5.94-11	5	2.00-10	6	3.81-10	7	7.85-10	8	1.48-9	9	2.18-9	9
8 GI contents	1.26-11	3	2.80-11	3	7.67-11	3	2.52-10	3	5.08-10	3	1.13-9	4	2.09-9	4	2.86-9	4
9 GI small int & contents	7.48-12	3	2.01-11	3	5.98-11	2	1.81-10	3	3.47-10	3	8.24-10	3	1.37-9	4	2.05-9	4
10 Heart	1.06-11	4	2.24-11	3	7.06-11	3	2.33-10	3	4.36-10	3	9.28-10	4	1.49-9	5	2.46-9	5
11 Kidney left	2.19-11	5	3.89-11	5	9.63-11	5	2.91-10	6	5.30-10	6	8.94-10	8	1.59-9	9	2.48-9	10
12 Kidney right	1.43-12	21	5.36-12	12	2.71-11	9	1.11-10	9	2.68-10	9	6.78-10	9	1.12-9	11	2.05-9	10
13 Liver	1.42-12	6	6.20-12	4	2.34-11	3	9.85-11	3	2.26-10	3	5.72-10	3	1.16-9	3	1.73-9	3
14 Lung left	1.79-11	2	3.38-11	2	9.73-11	3	2.67-10	3	4.82-10	4	9.04-10	4	1.51-9	5	2.43-9	5
15 Lung right	1.05-12	9	5.28-12	5	2.60-11	5	1.02-10	5	2.74-10	5	6.16-10	5	1.13-9	6	1.79-9	6
16 Ovary	1.40-12	49	9.88-11	27	1.06-11	34	1.04-10	36	1.46-10	47	4.62-10	42	9.79-10	46	4.74-10	97
17 Pancreas	1.10-11	9	2.45-11	7	7.00-11	8	2.02-10	9	3.81-10	11	8.78-10	13	1.79-9	13	2.28-9	16
18 Pelvis	1.98-11	2	3.12-11	2	5.93-11	2	1.75-10	3	3.20-10	3	6.42-10	4	1.26-9	4	1.96-9	4
19 Ribs	4.43-11	1	4.20-11	2	8.12-11	2	2.14-10	2	3.81-10	3	7.99-10	3	1.44-9	4	2.12-9	4
20 Scapulae	5.68-11	3	4.24-11	3	7.63-11	4	2.00-10	5	3.53-10	5	7.59-10	6	1.31-9	7	1.89-9	8
21 Spine	8.65-12	3	2.12-11	3	4.98-11	2	1.46-10	2	2.78-10	3	6.18-10	3	1.11-9	4	1.66-9	4
22 Skeleton	1.75-11	0.7	1.83-11	0.8	3.43-11	1	9.01-11	1	1.62-10	1	3.42-10	2	6.07-10	2	9.21-10	2
23 Skin trunk	3.12-11	1	3.64-11	1	9.63-11	2	2.72-10	2	4.88-10	2	9.59-10	3	1.65-9	3	2.50-9	3
24 Spleen	2.94-11	4	5.15-11	4	1.22-10	4	3.00-10	5	5.50-10	6	1.02-9	7	1.67-9	8	2.20-9	9
25 Thymus	3.78-12	21	1.46-11	16	4.98-11	15	1.27-10	19	4.12-10	17	6.62-10	22	1.74-9	21	2.31-9	24
26 Trunk average	1.78-11	0.2	2.62-11	0.3	6.82-11	0.2	2.03-10	0.2	3.87-10	0.2	8.26-10	0.3	1.44-9	0.4	2.22-9	0.4
27 Uterus	3.23-12	16	1.09-11	10	3.49-11	11	1.78-10	12	2.69-10	13	5.13-10	16	7.26-10	20	1.31-9	20

Table 12.5. Dose to some organs of the human body irradiated by a broad parallel beam of monoenergetic photons incident on the posterior of the torso

Organ	50 kev		100 kev		250 kev		660 kev		1.25 Mev		3 Mev		6 Mev		10 Mev	
	Dose (rads y^{-1} cm^2)	C of V (%)	Dose (rads y^{-1} cm^2)	C of V (%)	Dose (rads y^{-1} cm^2)	C of V (%)	Dose (rads y^{-1} cm^2)	C of V (%)	Dose (rads y^{-1} cm^2)	C of V (%)	Dose (rads y^{-1} cm^2)	C of V (%)	Dose (rads y^{-1} cm^2)	C of V (%)	Dose (rads y^{-1} cm^2)	C of V (%)
1 Adrenals	4.74-11	12	7.82-11	12	1.39-10	16	3.35-10	19	4.35-10	25	1.12-9	31	1.54-9	39	4.04-9	35
2 Bladder	1.16-11	13	2.72-11	10	7.45-11	12	2.21-10	14	4.86-10	16	1.40-9	17	1.83-9	20	2.54-9	24
3 Contents	9.02-12	10	2.46-11	7	7.43-11	7	2.19-10	8	3.94-10	9	9.47-10	10	1.51-9	11	2.69-9	11
4 Clavicles	9.03-12	17	1.74-11	12	3.25-11	15	9.64-11	18	3.27-10	16	4.32-10	22	1.05-9	21	1.85-9	21
5 G I stomach	1.38-11	7	3.51-11	6	8.11-11	7	2.45-10	8	4.90-10	9	1.07-9	10	2.17-9	11	2.39-9	14
6 G I U L I	1.32-11	6	3.38-11	5	8.02-11	6	2.61-10	7	4.99-10	7	8.17-10	10	1.58-9	11	2.23-9	12
7 G I L L I	1.74-11	6	4.12-11	5	1.11-10	6	2.95-10	7	4.63-10	9	1.10-9	10	1.59-9	12	2.72-9	13
8 G I contents	2.15-11	3	4.96-11	3	1.31-10	3	3.70-10	3	6.81-10	4	1.42-9	4	2.43-9	5	[illegible]	6
9 G I small int & contents	1.88-11	3	4.40-11	3	1.14-10	3	2.97-10	3	5.34-10	3	1.03-9	4	1.49-9	5	2.61-9	5
10 Heart	1.14-11	5	3.03-11	4	7.79-11	4	2.50-10	4	4.43-10	5	8.80-10	6	1.29-9	7	2.38-9	7
11 Kidney left	6.19-11	4	7.69-11	5	1.83-10	5	4.42-10	7	6.21-10	9	9.41-10	12	1.61-9	13	2.56-9	14
12 Kidney right	5.87-11	5	7.52-11	5	1.83-10	5	4.08-10	7	6.67-10	8	1.14-9	11	1.95-9	12	3.99-9	11
13 Liver	2.54-11	2	4.43-11	2	1.07-10	2	3.15-10	2	5.41-10	3	9.81-10	3	1.63-9	4	2.65-9	4
14 Lung left	2.60-11	3	4.60-11	3	1.23-10	3	3.28-10	4	5.22-10	5	9.26-10	6	1.64-9	7	2.80-9	7
15 Lung right	2.70-11	3	4.30-11	3	1.25-10	3	3.24-10	4	5.67-10	5	1.04-9	6	1.52-9	7	2.33-9	8
16 Ovaries	1.54-11	25	4.68-11	22	7.93-11	29	2.53-10	32	3.39-10	43	1.29-9	41	8.08-10	59	1.85-9	62
17 Pancreas	2.16-11	10	5.13-11	8	1.18-10	9	3.16-10	11	4.43-10	15	1.09-9	16	1.56-9	20	2.31-9	22
18 Pelvis	8.27-11	2	9.01-11	2	1.46-10	2	3.25-10	3	5.43-10	4	9.74-10	5	1.57-9	5	2.28-9	6
19 Ribs	7.97-11	2	7.15-11	2	1.15-10	2	2.91-10	3	5.10-10	3	9.49-10	4	1.57-9	5	2.20-9	5
20 Scapulae	1.27-10	3	9.83-11	3	1.67-10	4	3.44-10	5	6.23-10	6	9.88-10	8	1.64-9	9	3.00-9	9
21 Spine	6.57-11	2	8.35-11	2	1.36-10	2	3.02-10	3	4.53-10	3	9.18-10	4	1.41-9	5	2.08-9	5
22 Skeleton	3.74-11	0.7	3.96-11	0.8	6.66-11	1	1.50-10	1	2.57-10	2	4.66-10	2	7.84-10	2	1.12-9	2
23 Skin trunk	3.93-11	1	4.60-11	2	1.16-10	2	3.15-10	2	6.01-10	3	1.03-9	4	1.68-9	4	2.79-9	4
24 Spleen	4.65-11	5	7.12-11	5	1.57-10	5	3.60-10	7	5.68-10	8	1.13-9	10	2.00-9	11	2.14-9	14
25 Thymus	8.48-12	22	2.32-11	18	7.82-11	18	1.88-10	23	3.67-10	25	4.67-10	35	8.50-10	42	1.81-9	36
26 Trunk average	1.66-11	0.2	5.10-11	0.3	1.19-10	0.3	3.12-10	0.4	5.44-10	0.4	1.04-9	0.5	1.70-9	0.6	2.56-9	0.7
27 Uterus	1.04-11	13	2.97-11	9	8.08-11	11	2.00-10	14	2.88-10	17	7.58-10	18	1.45-9	20	1.53-9	25

1148009

Table 12.6. Effective Z for photon interactions in skeleton, lung, and soft tissue

Medium$_i$	i	Photoelectric		Compton		Pair production	
		$Z_{eff(i)}$	$Z_{eff(i)}/Z_{eff(1)}$	$Z_{eff(i)}$	$Z_{eff(i)}/Z_{eff(1)}$	$Z_{eff(i)}$	$Z_{eff(i)}/Z_{eff(1)}$
Soft tissue	1	6.41	1.00	3.34	1.00	4.58	1.00
Lung	2	6.59	1.03	3.44	1.03	4.75	1.04
Skeleton	3	7.58	1.18	3.88	1.16	5.21	1.14

The variation of dose for unilateral exposure to the left side of the body is shown in Fig. 12.11 for a traverse through the lower abdomen and a traverse through the chest region of the body. It may be noted that there is a leveling effect of dose across the lungs because of the low density there and the long mean flight paths of photons. It appeared that there was a slight increase in dose to tissue behind the right lung for several energies, and, since the lungs had an atomic composition slightly different from that of soft tissue, it was assumed that the increase was due to greater absorption coefficient values in tissue. According to Evans,[5] Compton scattering varies with atomic number, the photoelectric effect varies according to the fifth power of the atomic number, and pair production varies with the square of the atomic number. From this and the atomic composition of the different media, effective Z's for photoelectric, Compton, and pair production reactions in skeleton, lung, and soft tissue were computed, with the results shown in Table 12.6. Important reactions were Compton and photoelectric, which contribute equal amounts for $Z = 5$ and $E = 20$ keV; for energies below about 3 MeV, pair production is insignificant; however, effective Z's were computed for all reactions for the sake of completeness.

From Table 12.6, one would not expect a dose buildup in the tissue behind the right lung; therefore, the number of photon histories was increased by a factor of 4 in order to decrease the coefficient of variation by a factor of 2. The 660-keV case, the worst offender (as seen in Fig. 12.11), was recomputed. This calculation indicated that the dose curve was very flat across this region and that the previous apparent increase was purely a statistical phenomenon. For cases where the coefficients of variation are greater than about 0.20, problems indicate the existence of a nonnormal distribution because of the limited number of contributions. This is especially true for very small volumes such as the ovaries, where there are few contributing photon interactions.

5. R. D. Evans, *The Atomic Nucleus*, McGraw-Hill, New York, 1955.

Table 12.7 contains doses to red and yellow marrow in the human torso for the three exposure situations. Ribs of the skeletal approximation are closed and symmetrical; hence, doses to marrow of this region for anterior and posterior exposure are nearly identical. A depth-dose value equal to that for a penetration depth of 5 cm is commonly used by therapists for the dose to red marrow. Table 12.8 compares this assumption with the exposure situations from these calculations, and the assumption does not seem to be acceptable according to these results.

MEASUREMENTS OF DOSE DISTRIBUTIONS

Dose as a Function of Depth in a Tissue-Equivalent Phantom

A study was made of the dose deposited by fast neutrons at various depths in a tissue-equivalent phantom 30 cm in diameter and 60 cm high to simulate the human body. These measurements were intended to overcome several shortcomings in previous work as outlined by Hubbell and Auxier.[6]

The radiation sources used were the HPRR and a 14-MeV neutron generator. Doses due to recoil ions from neutron interactions and to gamma rays were measured separately. The gamma-ray doses measured for 14-MeV neutrons incident were those produced by neutron interactions in the phantom. For the HPRR case, the gamma-ray doses measured were due to neutron interactions in the phantom plus gamma rays from fission in the reactor core. In both cases, the doses due to neutrons and gamma rays scattered into the phantom from the surroundings were separately measured and subtracted. A gamma-ray dosimeter[7] having low neutron sensitivity was used, and the neutron detector was a small cyclopropane-filled proportional counter[8] of special design. Curves were plotted of the

6. H. H. Hubbell, Jr., and J. A. Auxier, "Review of Neutron Depth Dose Theory and Experiments," Health Physics Annual Meeting, Pittsburgh, Pennsylvania, June 1969.

7. E. B. Wagner and G. S. Hurst, *Health Phys.* 5, 20 (1961).

8. W. A. Mills and G. S. Hurst, *Nucleonics* 12(8), 33 (1954).

1148010

Table 12.7. Dose to bone marrow in the human torso irradiated by a broad parallel beam of monoenergetic photons incident on the anterior of the torso

		50 kev		100 kev		250 kev		660 kev		1.25 Mev		3 Mev		6 Mev		10 Mev	
		Dose (rads y^{-1} cm^2)	C of V (%)	Dose (rads y^{-1} cm^2)	C of V (%)	Dose (rads y^{-1} cm^2)	C of V (%)	Dose (rads y^{-1} cm^2)	C of V (%)	Dose (rads y^{-1} cm^2)	C of V (%)	Dose (rads y^{-1} cm^2)	C of V (%)	Dose (rads y^{-1} cm^2)	C of V (%)	Dose (rads y^{-1} cm^2)	C of V (%)
	Red and yellow marrow																
1	arm left	7.21-11	4	6.60-11	5	1.26-10	5	3.21-10	6	5.35-10	9	8.27-10	9	1.37-9	11	2.56-9	10
2	arm right	6.87-11	4	6.87-11	5	1.21-10	5	3.47-10	6	5.15-10	9	1.10-9	8	1.76-9	10	2.55-9	10
3	clavicles	9.67-11	6	6.93-11	7	1.20-10	9	2.53-10	12	4.82-10	17	8.76-10	16	1.14-9	21	2.15-9	21
4	pelvis	2.78-11	3	4.91-11	3	8.93-11	3	2.29-10	4	4.03-10	5	8.08-10	5	1.49-9	5	2.22-9	6
5	ribs	8.26-11	2	7.42-11	2	1.11-10	2	2.89-10	3	4.90-10	5	8.81-10	4	1.55-9	5	2.34-9	5
6	scapulae	1.97-11	6	3.25-11	5	6.74-11	6	1.96-10	7	3.95-10	9	7.90-10	9	1.46-9	10	2.03-9	11
7	spine lower	1.07-11	8	3.50-11	6	7.09-11	6	2.04-10	6	3.58-10	10	8.50-10	8	1.27-9	10	2.44-9	10
8	spine middle	1.25-11	5	3.39-11	4	6.52-11	4	1.81-10	4	3.30-10	6	7.47-10	5	1.25-9	6	2.01-9	6
	Yellow marrow only																
9	arm lower left	8.37-11	3	7.48-11	3	1.49-10	4	3.64-10	4	5.85-10	6	1.21-9	6	1.92-9	7	2.87-9	7
10	arm lower right	7.67-11	3	7.28-11	3	1.32-10	4	3.31-10	4	5.68-10	7	1.06-9	6	1.78-9	7	2.50-9	8
	Dose to Bone Marrow in the human Torso irradiated by a broad, parallel, beam of monoenergetic photons incident on the posterior of the torso																
	Red and yellow marrow																
1	arm left	7.09-11	4	6.62-11	5	1.21-10	5	3.22-10	6	6.01-10	7	1.01-9	9	1.53-9	10	2.34-9	11
2	arm right	6.70-11	4	6.62-11	5	1.12-10	5	3.01-10	6	4.70-10	7	1.08-9	8	1.94-9	9	2.59-9	11
3	clavicles	9.03-12	17	1.74-11	12	3.25-11	15	9.64-11	18	3.27-10	16	4.32-10	22	1.05-9	21	1.85-9	21
4	pelvis	8.27-11	2	9.01-11	2	1.46-10	2	3.24-10	3	5.43-10	4	9.74-10	5	1.57-9	5	2.29-9	6
5	ribs	7.98-11	2	7.16-11	2	1.15-10	2	2.91-10	3	5.10-10	3	9.50-10	4	1.57-9	5	2.20-9	5
6	scapulae	1.27-10	3	9.83-11	3	1.67-10	4	3.44-10	5	6.23-10	6	9.88-10	8	1.64-9	9	3.00-9	9
7	spine lower	8.25-11	3	9.72-11	3	1.62-10	4	3.77-10	5	5.39-10	6	1.02-9	8	1.78-9	9	2.54-9	10
8	spine middle	7.40-11	2	9.56-11	2	1.54-10	3	3.41-10	3	5.27-10	4	1.09-9	5	1.61-9	6	2.42-9	6
	Yellow marrow only																
9	arm lower left	8.01-11	3	8.65-11	3	1.52-10	3	3.14-10	4	6.66-10	5	9.30-10	7	2.00-9	7	2.45-9	8
10	arm lower right	7.34-11	3	6.89-11	3	1.29-10	4	3.01-10	5	5.55-10	5	1.07-9	6	1.98-9	7	2.69-9	8
	Dose to Bone Marrow in the human Torso irradiated by a broad, parallel, beam of monoenergetic photons incident on the left side of the torso																
	Red and yellow marrow																
1	arm left	1.15-10	2	9.43-11	1	1.54-10	3	3.57-10	4	5.83-10	5	1.04-9	6	1.64-9	7	2.44-9	7
2	arm right	2.29-13	38	1.84-12	16	7.13-12	13	4.60-11	10	1.34-10	9	4.57-10	9	7.40-10	10	1.18-9	10
3	clavicles	2.40-11	7	2.28-11	8	4.16-11	10	1.21-10	11	2.49-10	13	6.51-10	13	1.11-9	15	1.43-9	17
4	pelvis	1.98-11	2	3.12-11	2	5.93-11	3	1.75-10	3	3.20-10	3	6.42-10	4	1.26-9	4	1.96-9	4
5	ribs	4.43-11	1	4.21-11	2	8.12-11	2	2.14-10	2	3.81-10	3	7.99-10	3	1.44-9	4	2.12-9	4
6	scapulae	5.68-11	3	4.24-11	3	7.63-11	4	2.00-10	5	3.53-10	5	7.59-10	6	1.31-9	7	1.89-9	8
7	spine lower	9.58-12	6	2.38-11	5	5.75-11	5	1.51-10	5	3.01-10	6	7.67-10	6	1.38-9	7	1.79-9	8
8	spine middle	1.00-11	4	2.38-11	3	5.71-11	3	1.76-10	3	3.30-10	3	7.06-10	4	1.25-9	4	2.01-9	4
	Yellow marrow only																
9	arm lower left	1.26-10	1	9.93-11	2	1.54-10	2	3.41-10	3	5.54-10	4	1.05-9	4	1.78-9	5	2.69-9	5
10	arm lower right	2.06-13	11	1.48-12	14	7.11-12	10	3.65-11	8	1.15-10	8	3.86-10	7	7.73-10	7	1.37-9	7

1148011

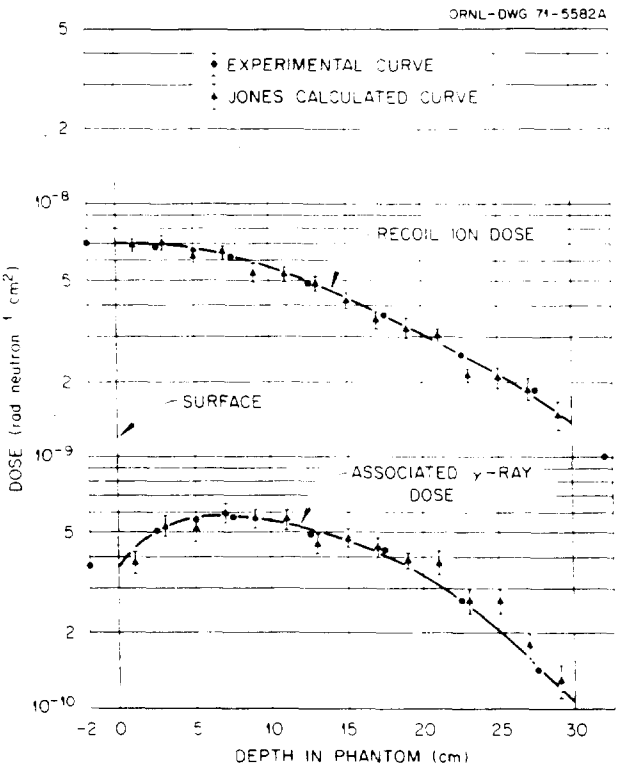

Fig. 12.12. Comparison of experimental depth-dose distributions for 14-MeV neutrons with calculations of T. D. Jones.

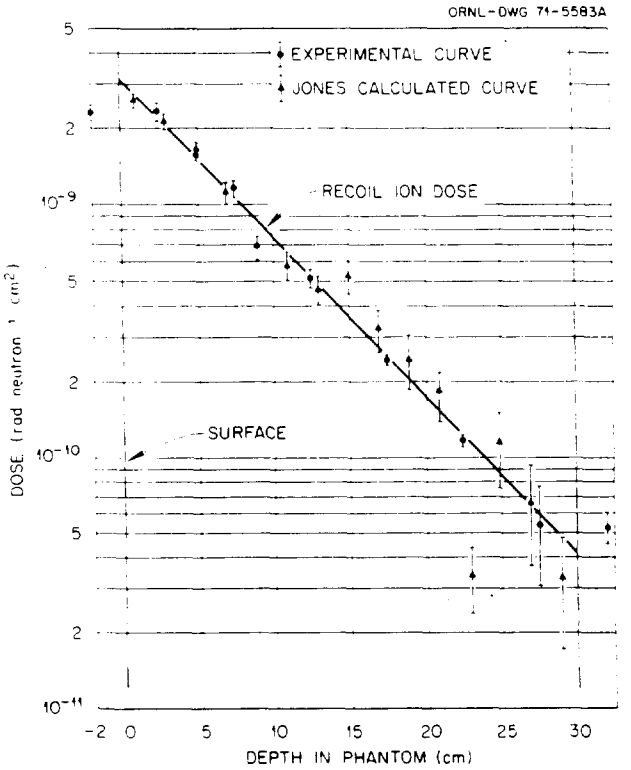

Fig. 12.13. Comparison of experimental depth-dose distribution for HPRR neutrons with calculations of T. D. Jones.

Table 12.8. Ratio of dose at a depth of 5 cm to average red marrow dose

Energy	Anterior	Posterior	Left side
6 MeV	1.3	~1	1.3
1.25 MeV	1.6	0.7	1.8
250 keV	2.0	0.5	2.0
50 keV	2.5	0.1	3.0

dose as a function of depth along the center line of the phantom perpendicular to its axis. The experimental data were analyzed by the "least-squares" method and fitted to an empirical equation of the form

$$D(X) = \frac{D(r)\, r^2 B^{-X/L}}{(r+X)^2} ,$$

where $D(X)$ is the dose rate at a depth of X centimeters in the phantom, $D(r)$ is the dose rate in air at the front surface of the phantom, r centimeters from the source, X is the depth in centimeters in the phantom measured from the front surface, B is the dose buildup at the surface of the phantom, that is, the ratio of the dose measurement at the front surface of the phantom to the measurement in air at that point without the phantom, and L is the relaxation length in centimeters. For the HPRR fission neutrons, the value of B was found to be 1.60, and the value of L was found to be 7.27 cm. For 14-MeV neutrons, B was found to be 1.88, and L was found to be 15.97 cm. The experimental results were compared with dose distribution curves which were calculated by the Monte Carlo statistical method.[9] The experimental results agreed with calculations within the standard deviations of either method (see Figs. 12.12 and 12.13).

Dose Distributions at Bone-Tissue Interfaces

Detectors[10] which facilitate the measurement of dose distributions at subcutaneous bone-tissue interfaces in a tissue-equivalent phantom have been described. The detectors rely upon the extrapolation ionization principle suggested by Failla.[11] These detectors have been

9. J. A. Auxier et al., *Health Phys. Div. Annu. Progr. Rep. July 31, 1965*, ORNL-3849, p. 171.
10. J. W. Poston et al., *Health Phys. Div. Annu. Progr. Rep. July 31, 1970*, ORNL-4584, pp. 152–55.
11. G. Failla, *Radiology* 29, 202–15 (1937).

1148012

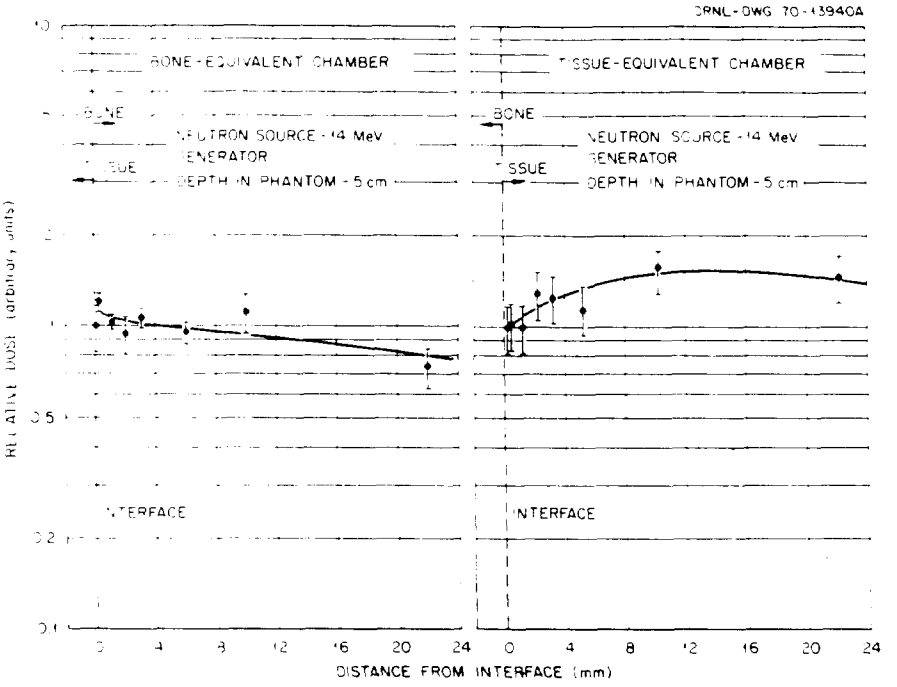

Fig. 12.14. Dose distribution in bone; dose distribution in tissue.

employed for measurement of dose distributions at bone-tissue interfaces due to incident fission neutrons from the HPRR.[10] The use of these detectors has been extended to measurements of distributions due to 14-MeV neutrons.

The DOSAR Low Energy Accelerator (DLEA) was the source of monoenergetic 14-MeV neutrons for this study. The experimental arrangement consisted of a standard[12] 30-cm cubical phantom filled with tissue-equivalent liquid[13] and located 0.50 m from the accelerator target. The center line of the phantom and the target were 0.96 m above the building floor. A Lucite tube, 5 cm in inside diameter with 0.635-cm-thick walls, was located along the center line of the phantom. This tube, which passes through the two parallel faces of the phantom, allows the movement of the ionization chambers through the phantom while isolating the detector from the liquid. Space in the tube not occupied by the detector is filled with tissue-equivalent material. Measurements were made only with the interface located at a depth of 5 cm. The interface was formed by use of tissue- and bone-equivalent plastics.[14,15]

Dose distributions near the interface resulting from a 14-MeV monoenergetic neutron source are shown in Fig. 12.14. These results are essentially as expected; there is an increase in the dose as the interface is crossed from bone into tissue. The buildup is about 50% at a depth of 9 to 10 mm in the tissue. In the bone environment, there is a reduction of about 20% at a depth of 20 mm. These distributions actually represent a summation of the neutron and gamma dose distributions near the interface since the ionization chambers have essentially equal sensitivity to both radiations. Comparison of these results to calculated neutron dose distributions will not be possible until the components of the distribution can be separated.

Initial Nuclear Radiation

Over the past decade the Radiation Shielding Subcommittee of the National Academy of Sciences' Advisory Committee on Civil Defense has developed extensive criteria and engineering methods for protection against fallout radiations. However, for the initial radiations, both neutrons and gamma rays, such

12. "Clinical Dosimetry," *Natl. Bur. Stand. (U.S.) Handb.* 87, U.S. Department of Commerce, 1963.

13. H. H. Rossi and G. Failla, *Nucleonics* 14, 32–37 (1956).

14. F. R. Shonka, J. E. Rose, and G. Failla, "Conducting Plastic Equivalent to Tissue, Air, and Polystyrene," pp. 160–66 in *Progr. Nucl. Energy, Ser. XII*, vol. 1, Pergamon, New York, 1959.

15. C. L. Wingate, W. Gross, and G. Failla, *Radiology* 79, 984–99 (1962).

1148013

criteria have been delayed because of the complexities of the problem and the lack of some important input data. Now it appears that the problem is manageable if the criteria are chosen properly. Two staff members of the Radiation Dosimetry Research Section were members of a "working group" picked by the subcommittee and given the responsibility of writing the criteria to be used as input in shielding calculations for the initial radiations from nuclear weapons.

A report of this study is published elsewhere[16] and is intended primarily for persons who are concerned with shielding for civil defense purposes and who are assumed to have a high degree of familiarity with this field. Typical of the recommendations and criteria given are:

1. A fission to fusion yield (energy) ratio of 50/50.
2. A "typical" intermediate thermonuclear neutron spectrum leaking from the weapon.
3. Because the direction to the detonation cannot be known in advance, the detonation is assumed to have occurred in a ring around the observer (equal probabilities in all directions).
4. The angular distribution of radiation at the shield be chosen such that the source would appear at an angle of elevation of 45° above the horizontal plane.
5. A source-detector distance of 1200 m in an infinite medium of air.

Information presented included source leakage spectra (neutron), neutron and gamma-ray spectra incident at the shield, energy and angular distributions and intensity relationships such as dose as a function of distance and source height, and peak overpressure as a function of weapon yield, height of burst, and distance.

16. J. A. Auxier, Z. G. Burson, R. L. French, F. F. Haywood, L. G. Mooney, and E. A. Straker, *Recommended Standard Free-Field Environment for Initial Radiation Shielding Calculations*, ORNL-TM-3396 (to be published).

1148014